

A New Bound on Axion-Like Particles

M.C. David Marsh¹, Helen R. Russell², Andrew C. Fabian²,
Brian R. McNamara^{3,4}, Paul Nulsen^{5,6}, Christopher S. Reynolds^{7,8}

¹ *Department of Applied Mathematics and Theoretical Physics,
University of Cambridge, Cambridge, United Kingdom*

² *Institute of Astronomy, University of Cambridge, Cambridge, United Kingdom*

³ *Department of Physics and Astronomy, University of Waterloo, Waterloo, Canada*

⁴ *Perimeter Institute for Theoretical Physics, Waterloo, Canada*

⁵ *Harvard-Smithsonian Center for Astrophysics, Cambridge, USA*

⁶ *ICRAR, University of Western Australia, Perth, Australia*

⁷ *Department of Astronomy, University of Maryland, College Park, USA*

⁸ *Joint Space-Science Institute (JSI), College Park, USA*

Axion-like particles (ALPs) and photons can quantum mechanically interconvert when propagating through magnetic fields, and ALP-photon conversion may induce oscillatory features in the spectra of astrophysical sources. We use deep (370 ks), short frame time *Chandra* observations of the bright nucleus at the centre of the radio galaxy M87 in the Virgo cluster to search for signatures of light ALPs. The absence of substantial irregularities in the X-ray power-law spectrum leads to a new upper limit on the photon-ALP coupling, $g_{a\gamma}$: using a very conservative model of the cluster magnetic field consistent with Faraday rotation measurements from M87 and M84, we find

$$g_{a\gamma} < 2.6 \times 10^{-12} \text{ GeV}^{-1}$$

at 95% confidence level for ALP masses $m_a \leq 10^{-13}$ eV. Other consistent magnetic field models lead to stronger limits of $g_{a\gamma} \lesssim 1.1\text{--}1.5 \times 10^{-12} \text{ GeV}^{-1}$. These bounds are all stronger than the limit inferred from the absence of a gamma-ray burst from SN1987A, and rule out a substantial fraction of the parameter space accessible to future experiments such as ALPS-II and IAXO.

December 8, 2017

Contents

1	Introduction	1
2	M87 and the Virgo cluster	4
2.1	Data reduction	4
2.2	Nuclear X-ray spectrum	7
3	Modelling the Virgo cluster	8
3.1	The gas density distribution	9
3.2	The Virgo magnetic field	10
3.3	Magnetic field model	12
4	ALP-photon conversion	14
4.1	ALP-photon conversion	14
4.2	Spectral distortions of M87 from ALPs	16
5	Parameter constraints	17
5.1	Method	18
5.2	Results	18
6	Conclusions	20
A	Sensitivity to background subtraction and modelling assumptions	21
A.1	Profile likelihood constraints and over-fitting	21
A.2	Bayesian model comparison	23
A.3	Magnetic field modelling sensitivity	25
A.4	Cluster background subtraction	27

1 Introduction

Symmetry is key in the modern understanding of fundamental physics, and the universe may support additional symmetries that have yet to be discovered. A promising route to search for new symmetries is to search for the remnants of broken symmetries. A spontaneously broken exact (global) symmetry results in a massless scalar particle called a Nambu-Goldstone boson; if the symmetry is only approximate, the resulting particle is a naturally light pseudo-Nambu-Goldstone boson [1]. A well-known example of a pseudo-Nambu-Goldstone boson is the QCD axion arising from the breaking of a new, postulated $U(1)$ Peccei-Quinn symmetry [2–4]. The axion may explain the

absence of detectable amounts of CP violation from the strong interactions, thereby solving the the ‘strong CP-problem’.

Axion-like particles (ALPs), here denoted a , are a class of pseudo-Nambu-Goldstone bosons that couple to electromagnetism through the interaction,

$$\mathcal{L}_{\gamma a} = -\frac{g_{a\gamma}}{4} a F_{\mu\nu} \tilde{F}^{\mu\nu} = g_{a\gamma} a \vec{E} \cdot \vec{B}, \quad (1.1)$$

where the ALP-photon coupling $g_{a\gamma}$ has dimension of inverse energy. Much of the low-energy phenomenology of ALPs is captured by only two parameters [5, 6]: $g_{a\gamma}$ and the ALP mass m_a , which can naturally be small compared to other particle physics mass scales.

In the presence of background magnetic fields, equation (1.1) induces quantum mechanical oscillations between photons and ALPs. Generically, the stronger and more coherent the magnetic field, the larger the probability of interconversion. Very strong magnetic fields that are coherent over laboratory scales are used in many experimental searches for axions (for a recent review, see [7]). Astrophysical magnetic fields that are coherent over substantially larger scales have been used to derive strong constraints on the axion-photon coupling. For example, the absence of an associated gamma-ray burst from supernova 1987A (SN1987A) has been shown to imply $g_{a\gamma} \lesssim 5.3 \times 10^{-12} \text{ GeV}^{-1}$ for light ALPs with $m_a \lesssim 4.4 \times 10^{-10} \text{ eV}$ [8–10]. For reviews of experimental and astrophysical axion and ALP bounds, see [11–13].

Galaxy clusters are extremely efficient converters of ALPs and photons with energies $\omega \gtrsim \mathcal{O}(\text{keV})$ [14–18] (see also [19–25]). The conversion probability is energy dependent and exhibits quasi-oscillatory features [16, 23]. ALP-photon conversion then leads to energy-dependent distortions of the photon spectrum of astrophysical sources, e.g. active galactic nuclei (AGN), located within or behind a galaxy cluster. The absence of large spectral distortions in the spectra of localised sources can be used to constrain the axion-photon coupling, $g_{a\gamma}$. Applying this approach to *Chandra* observations of the central AGN of the Hydra A cluster, reference [22] found the bound $g_{a\gamma} < 8.3 \times 10^{-12} \text{ GeV}^{-1}$ for $m_a < 7 \times 10^{-12} \text{ eV}$. More recently, reference [26] used *Chandra* observations of the AGN NGC1275 in the Perseus cluster to derive the bound $g_{a\gamma} \lesssim 3.8\text{--}5.9 \times 10^{-12} \text{ GeV}^{-1}$ for $m_a \lesssim 10^{-12} \text{ eV}$.¹ However, neither of these sources are ideal for deriving constraints on axion-like particles from existing observational data: Hydra A is a rather distant cluster, and possible modulations due to ALPs are hard to disentangle from statistical fluctuations and absorption features induced by the dense gas close to the source. For *Chandra* observations of NGC1275, the nuclear spectrum

¹Optimistic models of the cluster magnetic field then lead to stronger bounds. For NGC1275 in Perseus, some magnetic field models give $g_{a\gamma} \lesssim 2 \times 10^{-12} \text{ GeV}^{-1}$ [26].

is piled up (strongly so, for a substantial fraction of the observations) with multiple photons arriving at the same detector location in the same frame integration time. These photons are then confused with a single, more energetic photon or potentially a cosmic ray and then either excluded by the data reduction pipeline or not telemetered to the ground from the satellite. This makes it challenging to unambiguously associate spectral features with new, non-standard physics. Moreover, the magnetic field in both the Perseus and Hydra A clusters are not well known, which makes the rate of ALP-photon conversion uncertain [26].

In this paper, we derive constraints on $g_{a\gamma}$ from the absence of large distortions of the spectrum of the the central AGN of M87 in the Virgo cluster. This source is ideal for several reasons: at a distance of 16.1 Mpc, Virgo is the closest galaxy cluster to earth. This has made precision studies of the gas structure of Virgo possible, and *ROSAT*, *XMM-Newton* and *Chandra* have mapped out the electron density of the cluster with high resolution [27–29]. The central galaxy of the Virgo cluster, M87, hosts a supermassive black hole which appears as a very bright central X-ray point source and a jet. M87 was observed for a large *Chandra* program with a short frame time to mitigate the impact of pile-up and provide a very deep, clean spectrum of the central AGN. Moreover, the magnetic field in Virgo has been studied using rotation measurements, indicating a strong cluster magnetic field with a central value of $B_0 \approx 35\text{--}40 \mu\text{G}$ [30–32]. As we will show, this makes ALP-photon conversion unsuppressed at X-ray energies for a significant portion of the available parameter space. In combination, these factors allow us to derive the strongest bounds to date on light axion-like particles from *Chandra* observations of M87.

Under conservative assumptions of the magnetic field structure, we find that the absence of large irregularities in the X-ray spectrum of M87 leads to a new upper bound on $g_{a\gamma}$ for ALPs with $m_a < 3 \times 10^{-12} \text{ eV}$. For very light ALPs with $m_a < 10^{-13} \text{ eV}$, we find,

$$g_{a\gamma}|_{B_0=31.5\mu\text{G}} < 1.5 \times 10^{-12} \text{ GeV}^{-1} \quad (\text{at } 95\% \text{ c.l.}). \quad (1.2)$$

We verify that this bound is insensitive to uncertainties in the cluster background subtraction. Modifications of the cluster magnetic field model (including the central magnetic field strength and its radial fall-off) can change the derived limit by up to $\sim 75\%$; we consider several modifications to the magnetic field model and find that the weakest limit on $g_{a\gamma}$ to be given by,

$$g_{a\gamma}|_{B_0=35\mu\text{G}} < 2.6 \times 10^{-12} \text{ GeV}^{-1} \quad (\text{at } 95\% \text{ c.l.}). \quad (1.3)$$

This paper is organised as follows: in section 2 we discuss the observational data used in this analysis, and in section 3 we discuss our models for the cluster magnetic

field and electron density. In section 4 we review the physics of ALP-photon conversion, and in section 5 we present our new parameter constraints. We present our conclusions in section 6. In Appendix A, we compare the Bayesian parameter constraints with those obtained using the frequentist’s profile likelihood method, and we discuss the sensitivity of the constraints to the cluster gas properties and the magnetic field model.

2 M87 and the Virgo cluster

M87 has been observed frequently by the *Chandra* X-ray Observatory to study the nuclear and jet activity, the hot gas atmosphere and the population of low mass X-ray binaries. However, the bright nuclear point source is heavily piled up in observations using *Chandra’s* standard 3.1 s frame integration time. Pile-up occurs when multiple photons arrive in the same detector region within the same frame integration time and are therefore detected as a single photon event [33]. The photon energies sum to make a detected event of higher energy, which distorts the source spectrum, and the irregular shape of the charge cloud on the detector causes grade migration, where events are misidentified as cosmic rays and excluded. A shorter frame integration time of 0.4 s is required to reduce pile-up of the nucleus to at most a few per cent for M87.

The centre of M87 was observed with a short 0.4 s frame time for a total of 330 ks, split over nine observations, as a Cycle 17 Large Project (PI Russell). In addition to this new dataset, we also utilized all 0.4 s frame time observations of M87 in the *Chandra* archive taken since 2010. This results in an additional sixteen observations each of ~ 5 ks. Intense flaring of the jet knot HST-1, located only 0.85 arcsec from the nucleus, resulted in strong pile-up even in 0.4 s frame time observations taken between 2004 and 2010 [34]. The observations used in this analysis are detailed in Table 1. Extraction of the nuclear spectrum from the background cluster emission follows the analysis of the *Chandra* archive observations of M87 in [29], which is summarised below.

2.1 Data reduction

All datasets were analysed with CIAO 4.8 and CALDB 4.7.2 supplied by the *Chandra* X-ray Center [35]. Level 1 event files were reprocessed for the latest gain and charge transfer inefficiency correction and then filtered to remove cosmic rays. Background light curves were extracted from each observation in a region free of point sources. These light curves were compared to identify any time periods with high background count rates due to flares. No major flares were found in any of the observations. The final cleaned exposure times are detailed in Table 1. The total cleaned exposure time is 371.5 ks. Blank-sky backgrounds were also generated for each dataset. The appropriate background dataset was reprocessed similarly to the corresponding observation,

Table 1. Details of the *Chandra* observations used for this analysis and the best-fit nuclear spectral model parameters. The nuclear spectrum was fitted with an absorbed powerlaw model PHABS(ZPHABS(POWERLAW)) over the energy range 0.5–7 keV. (1) *Chandra* observation ID, (2) observation date, (3) exposure time, (4) intrinsic absorption, (5) photon index, (6) unabsorbed 2–10 keV flux.

Obs. ID	Date	Exposure (ks)	Intrinsic n_{H} (10^{22} cm^{-2})	Γ	Flux (2 – 10 keV) ($10^{-12} \text{ erg cm}^{-2} \text{ s}^{-1}$)
11513	13/04/2010	4.7	0.04 ± 0.02	2.33 ± 0.08	$1.42^{+0.10}_{-0.09}$
11514	15/04/2010	4.5	0.03 ± 0.02	2.14 ± 0.09	1.4 ± 0.1
11515	17/04/2010	4.7	0.02 ± 0.02	2.20 ± 0.08	1.6 ± 0.1
11516	20/04/2010	4.7	< 0.02	$2.02^{+0.08}_{-0.07}$	$1.6^{+0.09}_{-0.11}$
11517	05/05/2010	4.7	0.07 ± 0.02	2.35 ± 0.08	1.5 ± 0.1
11518	09/05/2010	4.0	0.04 ± 0.02	2.3 ± 0.1	$1.15^{+0.10}_{-0.09}$
11519	11/05/2010	4.7	0.06 ± 0.02	2.4 ± 0.1	1.01 ± 0.08
11520	14/05/2010	4.6	0.09 ± 0.02	2.5 ± 0.1	1.00 ± 0.08
13964	05/12/2011	4.5	$0.05^{+0.03}_{-0.02}$	2.3 ± 0.1	1.16 ± 0.09
13965	25/02/2012	4.6	0.02 ± 0.02	$2.10^{+0.09}_{-0.08}$	1.4 ± 0.1
14973	12/03/2013	4.4	0.03 ± 0.02	2.3 ± 0.1	1.16 ± 0.09
14974	12/12/2012	4.6	0.03 ± 0.03	2.2 ± 0.1	$1.15^{+0.10}_{-0.09}$
16042	26/12/2013	4.6	< 0.02	$2.10^{+0.08}_{-0.05}$	$1.02^{+0.08}_{-0.07}$
16043	02/04/2014	4.6	< 0.02	$2.07^{+0.07}_{-0.05}$	$1.57^{+0.10}_{-0.09}$
17056	17/12/2014	4.6	0.04 ± 0.03	2.3 ± 0.1	$1.04^{+0.09}_{-0.08}$
17057	19/03/2015	4.6	0.03 ± 0.03	2.01 ± 0.09	1.6 ± 0.1
18232	27/04/2016	18.2	0.08 ± 0.02	2.29 ± 0.07	$0.70^{+0.04}_{-0.03}$
18233	23/02/2016	37.2	0.03 ± 0.01	2.27 ± 0.05	0.62 ± 0.02
18781	24/02/2016	39.5	0.04 ± 0.01	2.21 ± 0.05	0.67 ± 0.02
18782	26/02/2016	34.1	0.04 ± 0.02	2.21 ± 0.05	0.70 ± 0.03
18783	20/04/2016	36.1	0.05 ± 0.02	2.28 ± 0.05	0.55 ± 0.02
18836	28/04/2016	38.8	0.08 ± 0.02	2.27 ± 0.05	0.72 ± 0.02
18837	30/04/2016	13.7	0.04 ± 0.03	2.32 ± 0.09	$0.52^{+0.04}_{-0.03}$
18838	28/05/2016	56.3	0.04 ± 0.01	2.30 ± 0.05	0.50 ± 0.02
18856	12/06/2016	24.5	0.05 ± 0.02	2.30 ± 0.07	$0.50^{+0.03}_{-0.02}$

reprojected to the correct sky position and normalized to match the observed count rate in the 9.5 – 12 keV energy band. Point sources were identified using a hard energy

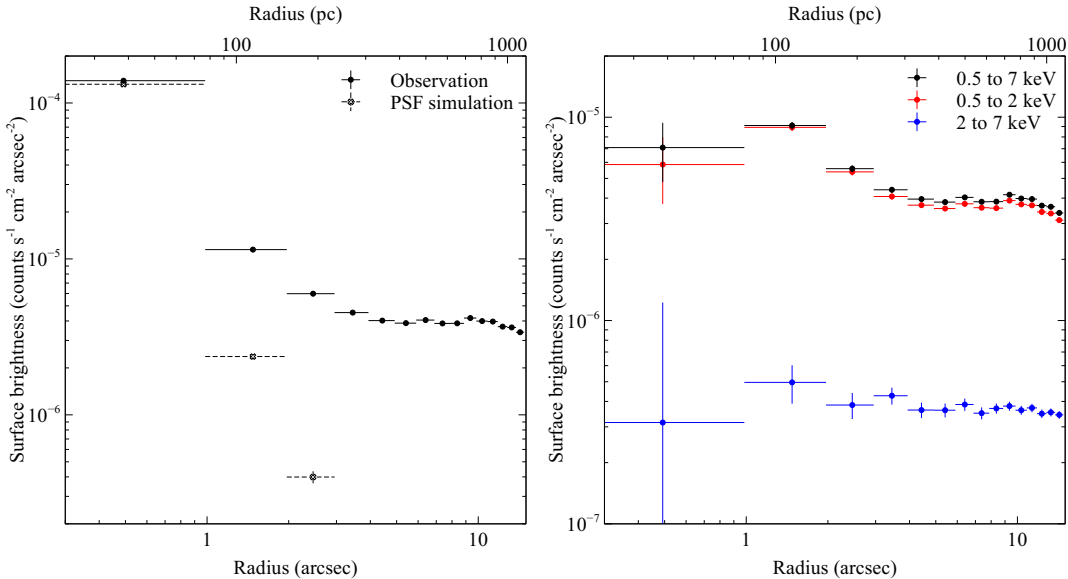


Figure 1. Left: Blank-sky background subtracted surface brightness profile from obs. ID 18838 together with a ChaRT/MARX simulation of the nuclear PSF. Both profiles used a 0.5–7 keV energy band. Right: PSF-subtracted cluster surface brightness profiles in the energy bands 0.5–7 keV, 0.5–2 keV and 2–7 keV.

band in each separate observation and a combined image and excluded as necessary. The emission from the jet was also carefully excluded.

The cluster background accounts for up to 10% of the emission within the region covered by the nuclear point spread function. Reference [29] showed that the cluster surface brightness increases towards the nucleus in M87, therefore a background spectrum extracted in a surrounding annulus will likely underestimate the true background. Following [29], we have therefore used a ChaRT/MARX PSF simulation to subtract the nuclear emission and evaluate the effect of the observed increase in the background cluster surface brightness. The stellar population and unresolved low mass X-ray binaries contribute at most a few per cent of this background and are not considered further [36].

The nuclear flux in M87 has decreased over time, therefore the cluster background contribution is most significant for the most recent datasets. We therefore analysed the cluster contribution in a recent observation with the lowest nuclear flux (obs. ID 18838), which is also the longest individual observation. The spectrum of the nuclear point source was extracted in this observation using a circular region centred on the emission peak with a radius of 1 arcsec. An appropriate response and ancillary response was also generated. The cluster background was estimated using an annulus covering a

radial region from 2 to 4 arcsec centred on the point source. The high energy wings of the *Chandra* point spread function (PSF) prevent the use of a background region closer to the bright nucleus ([37]). The spectrum was restricted to the energy range 0.5–7 keV, grouped with a minimum of 20 counts per spectral bin and analysed in XSPEC version 12.9.0 [38]. An absorbed powerlaw model PHABS(ZPHABS(POWERLAW)) was fitted to the spectrum where the two absorption components account for the Galactic foreground absorption and the intrinsic absorption local to M87, respectively. The Galactic absorption was fixed to the measured HI column density of $1.94 \times 10^{20} \text{ cm}^{-2}$ ([39]). The best-fit photon index was 2.30 ± 0.05 , the intrinsic absorption was $(4 \pm 1) \times 10^{20} \text{ cm}^{-2}$ and the flux in the energy range 2–10 keV was $(0.50 \pm 0.02) \times 10^{-12} \text{ erg cm}^{-2} \text{ s}^{-1}$. Table 1 shows the results of equivalent analyses for each of the observations of M87 to demonstrate the decrease in nuclear flux and the consistency of the best-fit absorption and photon index parameters. Observation 18838 should therefore provide a conservative representation of the larger dataset.

From the best-fit spectral model and the source position on the detector, the ChaRT ray-tracing program [40] and the MARX software (version 5.3.2, [41]) were used to simulate an observation of the nuclear PSF. ChaRT produces ray-traces through the *Chandra* mirror model and MARX projects these ray-traces onto the ACIS-S detector. This combination provides an accurate simulation of the on-axis *Chandra* PSF to at least 10 arcsec [37]. Figure 1 (left) shows the observed surface brightness profile and the corresponding ChaRT/MARX simulation of the nuclear contribution. The simulated nuclear surface brightness profile was subtracted from the observed profile to reveal the background cluster contribution. Figure 1 (right) shows that the cluster surface brightness measured in a 2–4 arcsec region will underestimate the cluster background in the nuclear region within 1 arcsec. However, this increase in surface brightness is limited to the soft energy band (0.5–2 keV), which traces the cooler, denser X-ray gas at the cluster centre. The harder energy band at 2–7 keV primarily traces hotter, projected gas and therefore has a flat surface brightness profile. The ALP models considered here are primarily constrained in the 2–7 keV energy range. Therefore, the cluster background determined from 2 to 4 arcsec is sufficient. We test the effect of the uncertainty in the cluster background in section A.4.

2.2 Nuclear X-ray spectrum

For the ALP model analysis, the extracted nuclear spectrum and corresponding background spectrum for each observation were fitted together in XSPEC with an absorbed powerlaw model PHABS(ZPHABS(POWERLAW)) over the energy range 2–7 keV. The absorption components were fixed to the Galactic value and the best-fit intrinsic absorption value of $3.9 \times 10^{20} \text{ cm}^{-2}$ [29]. The χ^2 statistic was used to determine the

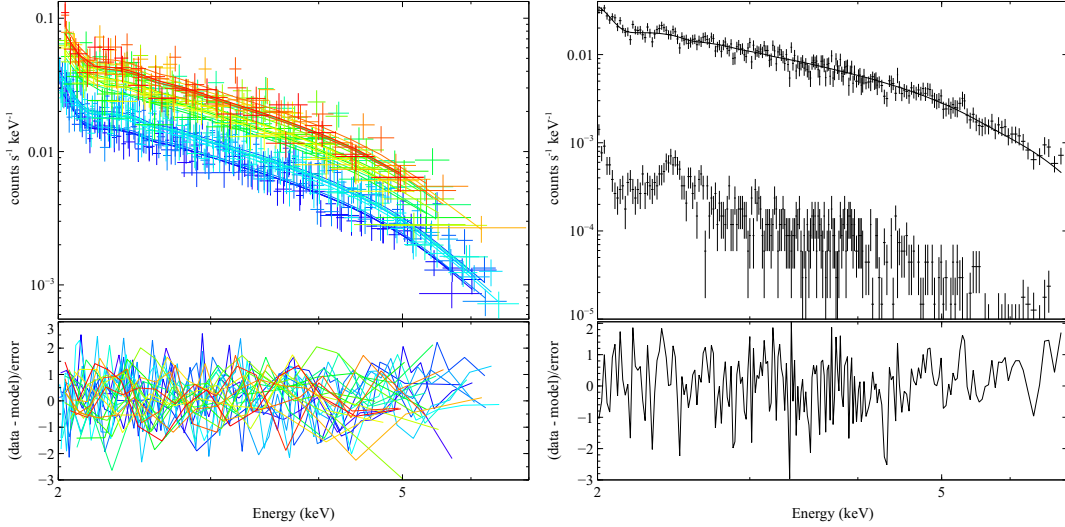


Figure 2. Left: Individual nuclear spectrum extracted from each of the 25 observations. Right: Summed spectrum of all observations taken in 2016 to demonstrate the data quality. The total exposure time is 298.4 ks. The background spectrum is also shown.

best-fit model. The photon index parameter was tied between the observations whilst the normalization was left free to account for the flux variability. The absorption and photon index do not appear to significantly vary over the six year time span of these observations (Table 1). Fig. 2 (left) shows the individual nuclear spectra from each observation. The best-fit photon index is 2.36 ± 0.03 , where $\chi^2 = 597.4$ for 614 degrees of freedom. Fig. 2 shows the nuclear spectrum summed over the observations taken in 2016 to more clearly demonstrate the data quality and the spectral fit. *Chandra's* effective area has changed significantly over the mission lifetime, therefore we can only sum observations taken at similar epochs. This summed spectrum and the corresponding spectral fit were therefore not used in our subsequent analysis. In section 5, we add the ALP-photon conversion model to the absorbed power-law model to place constraints on the ALP parameters m_a and $g_{a\gamma}$.

3 Modelling the Virgo cluster

Being nearby, bright and astrophysically rich, the Virgo cluster has been studied in great detail at radio, optical and X-ray wavelengths. As we discuss in this section, this makes it possible to construct observationally well-constrained models of the cluster magnetic field and gas density. In section 3.1, we briefly review existing *ROSAT*, *XMM-Newton* and *Chandra* determinations of the electron density of the intracluster

gas, and in sections 3.2 and 3.3 we discuss how multiple radio observations of the radio galaxies M87 and M84 can be used to constrain the galaxy cluster magnetic field.

3.1 The gas density distribution

The Virgo cluster is a ‘cool core’ cluster for which the cooling time of the X-ray emitting gas at the cluster centre is considerably smaller than the Hubble time, leading to a highly peaked surface brightness profile and the existence of a multi-temperature plasma at the centre of the cluster [42, 43]. The power output of the AGN at the centre of M87 sources a complex astrophysical environment with radio emitting lobes extending to distances of ~ 40 kpc from the jet (eg. [44–47]).

The gas density distribution has been studied by several X-ray satellites: reference [27] used *ROSAT* observations to determine the electron density within the central ~ 300 kpc region of M87; more recently, reference [28] collated 13 *XMM-Newton* pointings covering, on large scales, the Virgo cluster from its centre and northwards to radii beyond the cluster virial radius, $R_{\text{vir}} = 1.08$ Mpc; moreover, reference [29] used short frame time *Chandra* observations of M87 to determine the detailed gas density within the complicated, central 2 kpc region of M87 and resolve the gas density within the Bondi radius ($r \sim 0.2$ kpc) of the central black hole.

To model the Virgo cluster electron density, we use an interpolating spline model fitted to *Chandra* data obtained from [29] for $r < 19$ kpc, *ROSAT* data from [27] in the $19 \text{ kpc} < r < 298 \text{ kpc}$ region, and at large radii, $298 \text{ kpc} < r < 1080 \text{ kpc}$, we assume the scaling $n_e(r) \sim r^{-1.2}$ found by [28] to be accurate for $r \gtrsim 100$ kpc. Figure 3 shows the combined *Chandra* and *ROSAT* data together with the model of the electron density used in this paper.

X-ray images of the Virgo cluster reveal intrinsic asphericity on large scales, due to mergers with infalling small galaxy groups, and on small scales in M87 due to the AGN activity [45, 48]. However, for plausible limits on the axis ratio ($\pm 40\%$), the effects of large-scale triaxiality have been shown to be small, at typically less than a few per cent (see e.g. [49, 50]). On scales of a few kpc, radio jets and lobes powered by the central AGN displace the hot X-ray atmosphere, which produce larger uncertainties in the density profile. The model density profile interpolates over the affected regions (e.g. at a radius of 1.5 kpc in Figure 3). However, as discussed in section 4.2, the ALP-photon conversion probability is suppressed in the high-density cluster core, and asphericity in this region does not affect our bounds. In the bulk of the cluster, the uncertainty stemming from cluster asphericity is less important than the uncertainty in the cluster magnetic field, as we will now discuss.

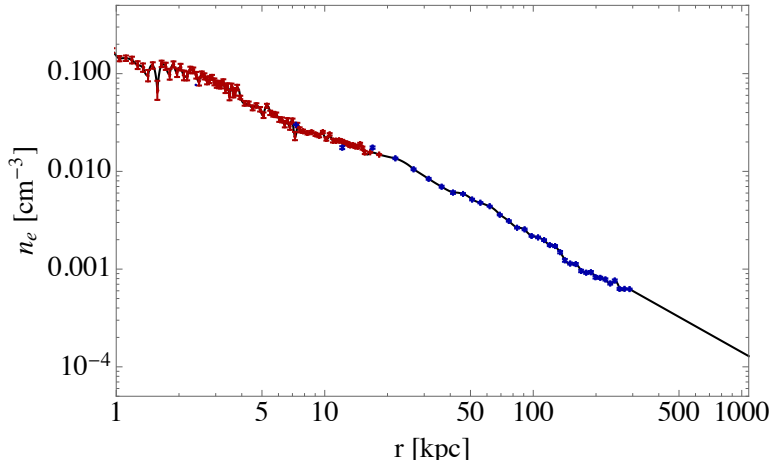


Figure 3. The Virgo deprojected electron density as observed by *Chandra* (red) and *ROSAT* (blue) [27]. Our model electron density (black line) is consistent with the large-radius scaling inferred from multiple *XMM-Newton* observations with $r \leq R_{\text{vir}}$ [28].

3.2 The Virgo magnetic field

A magnetised plasma, such as the Virgo intracluster medium, is birefringent and induces a wavelength-dependent rotation of the plane of polarisation of linearly polarised photons traversing it. This ‘Faraday rotation’ provides one of the main methods for inferring the magnetic field strength of galaxy clusters. The magnitude of the Faraday rotation is linearly proportional to the ‘rotation measure’, RM, which is given by the line-of-sight integral,

$$\text{RM} = \frac{e^3}{2\pi m_e^2} \int_{\text{l.o.s.}} n_e(l) \vec{B}(l) \cdot d\vec{l} = \frac{e^3}{2\pi m_e^2} \int_{\text{l.o.s.}} n_e(l) B_{\parallel}(l) dl. \quad (3.1)$$

With the electron density determined by X-ray observations, the statistical properties of the rotation measures from a source of polarised emission can be used to constrain the magnetic field in the ‘Faraday screen’ between the source and the observer.

Clearly, regions with a large electron density contribute comparatively more to the RM than low density regions. Moreover, for a statistically isotropic magnetic field, B_{\parallel} is uniformly distributed around zero and the average RM over several line-of-sights is zero.² The standard deviation $\sigma(\text{RM})$ of the rotation measures from an extended source indicates the typical magnitude of the RM. We here use observations of RMs from the radio galaxies M87 and M84 to constrain the Virgo cluster magnetic field.

²Conversely, a non-vanishing mean values of the RM over several sightlines indicate large-scale order in the magnetic field.

Observations of M87 have revealed very large rotation measures. Using four-frequency observations with the VLA, reference [30] found RMs of $\mathcal{O}(1000\text{--}2000)$ rad m^{-2} in the M87 lobes. Even larger RMs, $\mathcal{O}(4000\text{--}8500)$ rad m^{-2} , were found in a narrow filament, but the prominent jet region was found to give comparatively smaller RMs, $\mathcal{O}(300)$ rad m^{-2} . The large rotation measures were interpreted as arising from a Faraday screen in front of the synchrotron radiating, radio-emitting plasma, with most of the Faraday rotation occurring within a few kpc from the source, where the magnetic field strength was estimated to $B_0 \approx 40 \mu\text{G}$. In this interpretation, the lower rotation measures from the jet can be explained by the jet extending through and beyond the main Faraday screen.³

In reference [32], VLA data was used to infer the rotation measures of M87 with 0.4 arcsecond resolution, finding results largely consistent with reference [30]: the mean RM was found to range from around -1000 to 6000 rad m^{-2} , with typical values of $\mathcal{O}(1000)$ rad m^{-2} . Very large rotation measures $\mathcal{O}(3500\text{--}6000)$ rad m^{-2} were only found in a small region, and the jet was again found to be characterised by lower RMs $\mathcal{O}(100)$ rad m^{-2} . By approximating the RMs as a Gaussian, isotropic variable, the RM power spectrum was found to be flatter than anticipated by Kolmogorov turbulence. The magnetic field autocorrelation length was estimated to 0.2 kpc and the central magnetic field strength to $\mathcal{O}(35 \mu\text{G})$.

The large rotation measures observed in M87 should be contrasted with those observed in the radio galaxy M84, located around 400 kpc from the centre of Virgo. In reference [52], the magnitude of these were found to be 25–35 rad m^{-2} . Also in this case the origin of the rotation measures was interpreted to arise from the magnetised plasma within a few kpc from the source, as opposed to the bulk of Virgo cluster. We will find in section 3.3 that these observations provide highly complementary constraints on the cluster magnetic field to those inferred from rotation measures of M87.

We note in closing that cluster magnetic fields may in general have structure on scales \ll kpc which can be hard to infer from rotation measures. For example, kinetic-numerical simulations indicate that mirror and firehose instabilities driven by shear in the turbulent cluster plasma can generate field fluctuations of order $\delta B/B_0 \simeq 1$ on scales comparable to the ion Larmor radius [53], which is microscopic compared to the coherence scales inferred from rotation measures. As we explain in section 4.2, such

³Rotation measures from the M87 jet has been studied by several groups. Using VLBA observations at seven frequencies, reference [51] found rotation measures of $\mathcal{O}(9000)$ rad m^{-2} on milli-arc second scales. The extremely large RMs were interpreted as arising from very dense gas clouds near the central AGN. The M87 jet has further been studied on kiloparsec scales in reference [31] using four-frequency VLA data, where it was argued that the RMs in the jet is of a different origin than the RMs of the lobes.

small-scale structure is likely to have a negligible impact on the ALP-photon conversion rate from the cluster, and we do not attempt to capture these effects in our magnetic field model, which we now describe.

3.3 Magnetic field model

The complicated, tangled magnetic field of the Virgo cluster cannot be directly determined from astronomical observations, however, it is possible to construct models of the cluster magnetic field that are consistent with the observed Faraday rotation measures.

We model the cluster magnetic field along a given line-of-sight (that we here take to extend radially from the centre of the cluster) to consist of multiple domains of constant magnetic field,

$$\vec{B}(r) = \sum_{i=0}^N (\vec{B})_i(r), \quad (3.2)$$

where $(\vec{B})_i$ is only non-vanishing for $R_i < r < R_{i+1}$, and is constant over this domain. In each domain, the magnetic field is described by a random, isotropically distributed unit vector, $(\vec{b})_i$, multiplying a radial scaling function,

$$(\vec{B})_i = B_0 \left(\frac{n_e(r)}{n_e(0)} \right)^\alpha (\vec{b})_i, \quad (3.3)$$

where B_0 denotes the central magnetic field strength and α determines the fall-off of the magnetic field relative to the gas density.

Clearly, this simple model can only be expected to provide an approximation to the multi-scale structure and radial fall-off of the actual cluster magnetic field. Furthermore, Faraday rotation measures are only sensitive to the radial component of the magnetic field along the line-of-sight, cf. equation (3.1), while ALP-photon conversion depends on the perpendicular component, as we will discuss in section 4. A substantial non-isotropic component of the actual cluster magnetic at large radii may affect the rate of ALP-photon conversion.

The coherence lengths, $L_i = R_i - R_{i-1}$, may in general depend on the distance from M87. Close to the source, reference [32] suggests a magnetic field with an auto-correlation length of 0.2 kpc. We here model the region within 2 kpc from the central point source as consisting of 10 domains of equal length, i.e. $L_i = 0.2$ kpc for $1 \leq i \leq 10$. Outside this region, in the bulk of the Virgo cluster, we take the coherence lengths L_i to be independent and randomly distributed with a power-law probability distribution for all $i > 0$,

$$p(L_i) \sim \begin{cases} L_i^{-\gamma} & \text{for } L_i > L_{\min}, \\ 0 & \text{otherwise,} \end{cases} \quad (3.4)$$

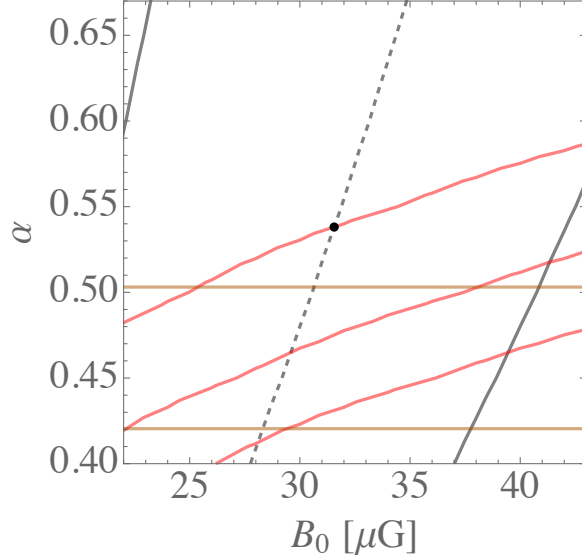


Figure 4. Parameter constraints from Faraday rotation measures. From left to right, grey curves indicate $\sigma(\text{RM}_{\text{M87}}) = 1000, 1500$ (dashed), 2000 rad m^{-2} . From top down, red curves indicate $\sigma(\text{RM}_{\text{M84}}^{\text{Virgo}}) = 5, 7.5, 10 \text{ rad m}^{-2}$ and orange horizontal lines indicate near-source contributions to the M87 RM of 85% and 80%. The black dot indicates our baseline parameters, $B_0 = 31.6 \mu\text{G}, \alpha = 0.54$.

We extend this model to the virial radius: $R_N \approx R_{\text{virial}} = 1.08 \text{ Mpc}$. The parameters of this model are then $(B_0, \alpha, \gamma, L_{\text{min}})$. Motivated by more elaborate modelling of the magnetic field in cool core galaxy clusters [54], we take $\gamma = 2.5$ and $L_{\text{min}} = 1 \text{ kpc}$ in our benchmark magnetic field model, and we constrain B_0 and α by the observed rotation measures from M87 and M84.

For the centrally located radio galaxy M87, we expect $\text{RM}_{\text{M87}} \approx \mathcal{O}(1000\text{--}2000)$. To determine the dependence of the rotation measures on the magnetic field model parameters, we simulate a large number of magnetic field realisations with a given set of parameters, (B_0, α) , and compute the standard deviation of the rotation measures from M87: $\sigma(\text{RM}_{\text{M87}})$. Contours of constant $\sigma(\text{RM}_{\text{M87}})$ in the relevant range are indicated by grey, almost vertical lines in Figure 4. According to the interpretation of reference [30], the Faraday rotation measures from M87 chiefly arises from the high gas density region with $r \lesssim r_* = 20 \text{ kpc}$, rather than the bulk of the Virgo cluster. This constrains the radial fall-off parameter, α . To estimate the typical near-source contribution to the rotation measure, we simulate many magnetic fields realisations for a given choice of B_0 and α and compute,

$$\mathfrak{f} = \text{median} \left| \frac{\text{RM}(R_{\text{vir}}) - \text{RM}(r_*)}{\text{RM}(r_*)} \right|, \quad (3.5)$$

where we used the notation $\text{RM}(r) = \frac{e^3}{2\pi m_e^2} \int_0^r n_e(l) B_{\parallel}(l) dl$. Contours with $f = 0.8$ and 0.85 are given by the orange, horizontal lines in Figure 4.

The magnetic field model is also constrained by the comparatively small rotation measures observed from M84. Similarly to the case of M87, the M84 rotation measures are expected to chiefly arise from the magnetised plasma within ~ 10 kpc from the source. More elaborate models of the local magnetic field and the gas density may be used to describe this region. Here however, we expect our model to capture the (subdominant) *galaxy cluster* contribution to the rotation measures from M84, $\text{RM}_{\text{M84}}^{\text{Virgo}}$, but not the (dominant) local contribution. We may then constrain a combination of B_0 and α by placing an upper bound on $\sigma(\text{RM}_{\text{M84}}^{\text{Virgo}})$, as illustrated by the red contours in Figure 4.

These constraints from rotation measurements from M87 and M84 do not uniquely determine the parameters B_0 and α . However, we note that if the energy density in the magnetic field scales with the energy density in the plasma, then $B^2 \sim n_e$ and $\alpha = 1/2$. Our baseline magnetic field model used in this paper takes $B_0 = 31.6 \mu\text{G}$, and $\alpha = 0.54$, consistent with the constraints from rotation measures and conservatively with respect to previous estimates of the central magnetic field strength. We discuss the sensitivity of ALP-photon conversion to this choice of parameters in Appendix A.

4 ALP-photon conversion

In this section, we describe the physics of ALP-photon conversion and our method to compute the photon survival probability for X-ray photons from M87.

4.1 ALP-photon conversion

In addition to the ALP-photon interaction (1.1), the ALP dependent contribution to the Lagrangian is given by,

$$\mathcal{L}_a = -\frac{1}{2} \partial_{\mu} a \partial^{\mu} a - \frac{1}{2} m_a^2 a^2. \quad (4.1)$$

To study ALP-photon conversion in galaxy clusters, it is convenient to linearise the equations of motion in a background with an external magnetic field, $\vec{B}(\mathbf{x})$, and a plasma with electron density $n_e(\mathbf{x})$. Upon neglecting the subleading effect of Faraday rotation, the equation of motion for a mode of energy ω propagating in the z -direction is given by [6],

$$\left((\omega - i\partial_z) \mathbb{I} + M(z) \right) \begin{pmatrix} |\gamma_x\rangle \\ |\gamma_y\rangle \\ |a\rangle \end{pmatrix} = 0, \quad (4.2)$$

where

$$M(z) = \begin{pmatrix} \Delta_\gamma(z) & 0 & \Delta_{\gamma ax}(z) \\ 0 & \Delta_\gamma(z) & \Delta_{\gamma ay}(z) \\ \Delta_{\gamma ax}(z) & \Delta_{\gamma ay}(z) & \Delta_a(z) \end{pmatrix}. \quad (4.3)$$

The quantum mechanical ALP-photon oscillations are induced by the off-diagonal matrix elements,

$$\Delta_{\gamma ai} = \frac{g_{a\gamma} B_i(\mathbf{x})}{2}. \quad (4.4)$$

Here $\Delta_\gamma = -\omega_{pl}^2/2\omega$ is determined by the plasma frequency $\omega_{pl}^2(\mathbf{x}) = 4\pi e^2 n_e(\mathbf{x})/m_e$, and $\Delta_a = -m_a^2/\omega$. The general solution to equation (4.2) is given by the path-ordered transfer matrix,

$$\begin{pmatrix} |\gamma_x\rangle \\ |\gamma_y\rangle \\ |a\rangle \end{pmatrix} (R) = \mathcal{P}_z \left[\exp \left(-i\omega R \mathbb{I} - i \int_0^R M(z) dz \right) \right] \begin{pmatrix} |\gamma_x\rangle \\ |\gamma_y\rangle \\ |a\rangle \end{pmatrix}_0. \quad (4.5)$$

When the matrix $M(z)$ can be approximated as piece-wise constant over the ranges $R_i \leq z < R_{i+1}$ for $i = 0, \dots, N$ (again denoting the coherence length by $L_i = R_i - R_{i-1}$), the full transfer matrix is simply given by,

$$\mathcal{P}_z \left[\exp \left(-i\omega R \mathbb{I} - i \int_0^R M(z) dz \right) \right] = e^{-i\omega R \mathbb{I}} \mathcal{P}_z \left(\prod_{i=1}^N e^{-iL_i M(R_i)} \right). \quad (4.6)$$

The probability that a photon that initially is linearly polarised along the x -direction is converted to an ALP after propagating from $z = 0$ to $z = R_N = R$ is then given by,

$$P_{\gamma_x \rightarrow a} = \left| (0, 0, 1) \mathcal{P}_z \left(\prod_{i=1}^N e^{-iL_i M(R_i)} \right) \begin{pmatrix} 1 \\ 0 \\ 0 \end{pmatrix} \right|^2. \quad (4.7)$$

The conversion probability for an unpolarised beam of photons is then given by $P_{\gamma \rightarrow a} = \frac{1}{2} (P_{\gamma_x \rightarrow a} + P_{\gamma_y \rightarrow a})$, and the photon survival probability is given by $P_{\gamma \rightarrow \gamma} = 1 - P_{\gamma \rightarrow a}$. Since $P_{\gamma_i \rightarrow a} = P_{a \rightarrow \gamma_i}$ and $P_{a \rightarrow a} + P_{a \rightarrow \gamma_x} + P_{a \rightarrow \gamma_y} = 1$, clearly $P_{\gamma_x \rightarrow a} + P_{\gamma_y \rightarrow a} \leq 1$ and $P_{\gamma \rightarrow \gamma} \geq 1/2$.

We close this subsection by discussing the possible impact of so-called ‘resonant’ conversion. For ALPs more massive than the effective photon mass ω_{pl} , photon-to-ALP conversion tends to be suppressed by $P_{\gamma \rightarrow a} \sim (\omega_{pl}/m_a)^4$. If somewhere in the cluster, $m_a \approx \omega_{pl}$, the conversion probability can become much larger. To see this, we may consider $P_{\gamma \rightarrow a}$ evaluated over a single domain of size L and with perpendicular magnetic field B_\perp :

$$P_{\gamma \rightarrow a} = \frac{1}{4} \frac{\Theta^2}{1 + \Theta^2} \sin^2 \left(\Delta \sqrt{1 + \Theta^2} \right), \quad (4.8)$$

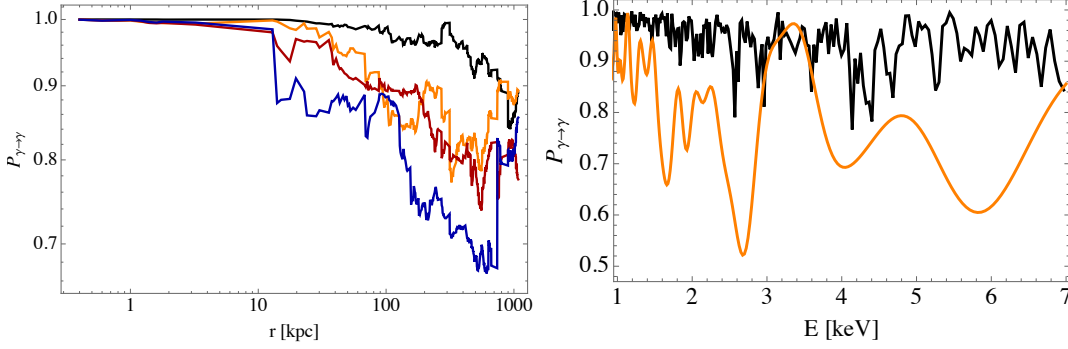


Figure 5. Left: Example of radial dependence of photon survival probabilities for $E = 1$ keV (black), 3 keV (orange), 5 keV (red) and 7 keV (blue) in a randomly generated magnetic field with benchmark parameters, and ALP parameters $m_a = 0$, $g_{a\gamma} = 5 \times 10^{-12}$ GeV $^{-1}$. Right: Example of energy dependence of survival probability for the same ALP parameters (orange), and for the same $g_{a\gamma}$ but with $m_a = 3.3 \times 10^{-12}$ eV (black).

where $\Theta = 2B_{\perp}\omega g_{a\gamma}/m_{\text{eff}}^2$, $\Delta = m_{\text{eff}}^2 L/(4\omega)$ and $m_{\text{eff}}^2 = m_a^2 - \omega_{\text{pl}}^2$. If $m_{\text{eff}}^2 \ll \omega_{\text{pl}}^2$ so that $\Theta \gg 1$, $\Delta \ll 1$ with $\Theta\Delta < 1$, the conversion probability can be ‘resonantly enhanced’ to,

$$P_{\gamma\rightarrow a} \approx \frac{1}{4}\Theta^2\Delta^2 = 1.2 \times 10^{-4} \left(\frac{B_{\perp}}{10 \mu\text{G}} \frac{L}{1 \text{ kpc}} \frac{g_{a\gamma}}{10^{-12} \text{ GeV}^{-1}} \right)^2. \quad (4.9)$$

We note that in the cluster, both ω_{pl} and B_{\perp} are not expected to be constant and regions in which $m_a^2 \approx \omega_{\text{pl}}^2$ are not very large.

In our numerical evaluation of the transfer matrix, we assume $\omega_{\text{pl}}(R_i)$ and $M(R_i)$ to be piece-wise constant over a set of domains. Only a limited set ALP masses will then satisfy $m_a^2 \approx \omega_{\text{pl}}^2(R_i)$ for all i , so that our numerical implementation neglects the resonant enhancement of the amplitude of intermediate masses. However, the error associated with this effect is negligibly small, cf. equation (4.9), which justifies our approach.

4.2 Spectral distortions of M87 from ALPs

Photons emitted from the bright, central source of M87 may convert into ALPs when propagating through the galaxy cluster magnetic field. In this section we briefly summarise the phenomenology of ALP-photon conversion in the Virgo cluster.

Substantial inter-conversion of ALPs and photons occur when the off-diagonal components of the matrix (4.3) are comparable to the diagonal terms. For massless ALPs, $\Delta_a = 0$, and the non-vanishing diagonal terms depend on the electron density of the environment and the energy of the particle, $\Delta_{\gamma} \sim n_e/\omega$. Hence, large electron densities

and low energies suppress the conversion probability. Consequently, in the cluster environment, both the radius at which the conversion becomes important and the overall conversion probability are energy dependent.

Figure 5 illustrates how, for a randomly generated magnetic field with benchmark parameters, the photon-to-ALP conversion probability is highly stochastic and exhibits quasi-oscillatory features. At small radii the conversion probability is suppressed over the entire X-ray range due to the large electron density close to the centre of the cluster. At radii $\gtrsim \mathcal{O}(10\text{--}100)$ kpc, ALP-photon conversion becomes important. Higher energy photons (for which the diagonal terms of (4.3) are more heavily suppressed) achieve large conversion probabilities at smaller radii than less energetic photons. A non-vanishing ALP mass suppresses the amplitude of the conversion and increases the frequency of the oscillations.

It is now clear why neglecting the small-scale structure of the magnetic field is well-motivated: to leading order, the ALP-photon amplitude from the i :th domain scales like $\sim g_{a\gamma} B_i L_i$, and the conversion probability scales like $\sim (g_{a\gamma} B_i L_i)^2$. Domains with $L_i \ll \text{kpc}$ provide suppressed contributions to the amplitude, and as such domains are expected to comprise a very small fraction of the cluster volume, their effects on the conversion probability can be neglected.⁴

Finally, we note that the bright point-like source at the centre of M87 in reality has a finite extent, and photons from different parts of the source travel along slightly different sight-lines to the detector. In general, well-separated sight-lines probe different magnetic fields, and the total cluster conversion probability becomes averaged, which suppresses the oscillatory features. This averaging effect becomes significant for sight-lines separated by $\mathcal{O}(\text{few})$ kpc [16]. As the point source at the centre of M87 is not much larger than $\mathcal{O}(10 \text{ pc})$ [55, 56], this effect is completely negligible in our case, and the single sight-line approximation is well justified.

5 Parameter constraints

We are now ready to compute the constraints on the ALP parameters $g_{a\gamma}$ and m_a from the absence of large spectral irregularities in the M87 X-ray spectrum. In this section, we marginalise over the unknown magnetic field profile to derive constraints on the ALP parameters. For a discussion of parameter constraints obtained using the profile likelihood method, a Bayesian model comparison, and a discussion on the sensitivity of the bound to modelling assumptions and data reduction uncertainties, we refer the reader to Appendix A.

⁴Similarly, small-scale magnetic fields have a very small effect on cluster rotation measures, which like the domain amplitude, are linear in the coherence length.

5.1 Method

We first note that the observed spectrum of the AGN is well-fitted by an absorbed power-law (giving $\chi^2 = 597.4$ for 614 degrees of freedom) in the 2–7 keV range, and exhibits no large, irregular features that immediately call for physics beyond the Standard Model.

To simulate the effects of an ALP on the observed AGN spectrum, we compute the survival probability function $P_{\gamma \rightarrow \gamma}(E)$ for photons propagating from M87 at the centre of the Virgo cluster to the virial radius, $R_{\text{vir}} = 1.08$ Mpc. The survival probability is a sensitive function of the ALP parameters and the randomly generated magnetic field: we here sample 270 parameter choices in the relevant region of the $(m_a, g_{a\gamma})$ parameter space, and, for each of these choices, compute $P_{\gamma \rightarrow \gamma}(E)$ for 100 randomly generated magnetic field profiles. Before entering the bulk of the Virgo cluster, the soft X-ray energy range (< 2 keV) of the power-law spectrum from the AGN gets modified by absorption in dense clouds near the black hole, resulting in an absorbed power-law spectrum that we denote by $I_0(E)$. The ALP-modified spectrum in the detector frame is given by,

$$I(E; b, m_a, g_{a\gamma}) = D^{\text{MW}}(E) P_{\gamma \rightarrow \gamma}(E(1+z); b, m_a, g_{a\gamma}) I_0(E(1+z)), \quad (5.1)$$

where b labels the random magnetic field profile and $D^{\text{MW}}(E)$ denotes the absorption in the Milky Way. Here z denotes the redshift to M87, $z = 0.0044$.

We used `FLX2TAB` in `XSPEC` to generate table models for each version of the ALP component. The absorbed power-law model was then multiplied by a redshifted ALP table model and this combined model, $I(E; b, m_a, g_{a\gamma})$, was then fitted to the observed spectrum. Our subsequent analysis of the result relies solely on the computed chi-square of each fit, $\chi^2(b, m_a, g_{a\gamma})$.

5.2 Results

To obtain a constraint on the ALP parameters $(m_a, g_{a\gamma})$, we marginalise over the unknown magnetic field profile, as parametrised by b . More precisely, under the assumption of approximate Gaussianity, we find the three-dimensional probability distribution $p(m_a, g_{a\gamma}, b)$, which is normalised so that $\sum_{m_a, g_{a\gamma}, b} p(m_a, g_{a\gamma}, b) = 1$. The marginalised probability distribution for the ALP parameters is then given by,

$$p(m_a, g_{a\gamma}) = \sum_b p(m_a, g_{a\gamma}, b). \quad (5.2)$$

Figure 6, which is the main result of this paper, shows the inferred 68% and 95% confidence regions in the ALP parameter space. We note that for light ALPs, the upper

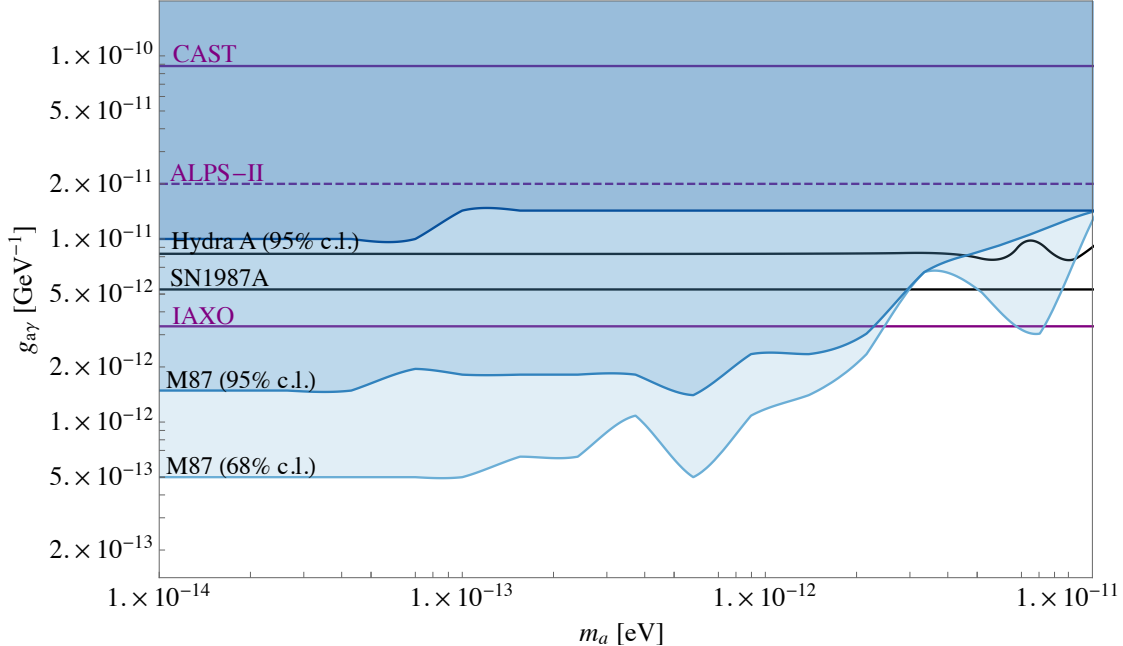


Figure 6. Parameter constraints at the 68% (light blue), 95% (middle blue) and 99.7% (dark blue) confidence levels. Coloured regions are excluded. Not plotted are constraints from NGC1275 which give $g_{a\gamma} \lesssim 3.8\text{--}5.9 \times 10^{-12} \text{ GeV}^{-1}$ for $m_a \lesssim 10^{-12} \text{ eV}^{-1}$ [26].

bound on the ALP-photon coupling derived here,

$$g_{a\gamma}|_{B_0=31.5\mu\text{G}} < 1.49 \times 10^{-12} \text{ GeV}^{-1}, \quad (5.3)$$

at 95% confidence level, is a factor of $\gtrsim 3$ stronger than the upper bound obtained from the analysis of SN987A [8–10]. We note that the transfer matrix only depends on the central magnetic field B_0 and $g_{a\gamma}$ through $\Delta_{\gamma ai}$, and that the transformation $B_0 \rightarrow \lambda B_0$, $g_{a\gamma} \rightarrow g_{a\gamma}/\lambda$ leaves the conversion probability invariant. Our benchmark constraint is derived for a conservative value of the central magnetic field ($B_0 = 31.5 \mu\text{G}$); should the actual magnetic field be stronger, our constraints would similarly be strengthened. For example, for a central magnetic field of $B_0 = 40 \mu\text{G}$ (as suggested by [30]), keeping all else fixed, our constraint translates into,

$$g_{a\gamma}|_{B_0=40\mu\text{G}} < 1.17 \times 10^{-12} \text{ GeV}^{-1}, \quad (5.4)$$

at 95% confidence level. As shown in Appendix A, these constraints are rather robust under modifications in the modelling of the magnetic field and the reduction of the observational data to take into account the cluster background.

6 Conclusions

In this paper we have used *Chandra* observations of the central point source of M87 in the Virgo cluster to search for light ALPs. X-ray photons emitted from the AGN may oscillate into ALPs in the cluster magnetic field. As the oscillation probability is energy dependent, this induces quasi-oscillatory features in the observed spectrum.

We consider 25 *Chandra* observations with a total clean exposure time of 371.5 ks, taken from 2010 to 2016. By only using observations with a short, 0.4 s, frame time, the effects of pile-up are minimal and the cleaned data is of high quality. We analyse the nuclear spectra using XSPEC and find that it is well fitted by an absorbed power law, accounting for the flux variability, and exhibits no substantial modulations that call for Beyond the Standard Model physics.

We construct models of the electron density and the magnetic field in the Virgo cluster that are consistent with X-ray and radio observations, and we use these models to simulate the effects of ALP-photon conversion from M87. As Virgo is a large cluster with a comparatively strong magnetic field, ALP-photon conversion is unsuppressed in a large region of the observationally allowed parameter space. We translate the absence of large modulations in the X-ray spectrum into constraints on the ALP parameters $(m_a, g_{a\gamma})$. Our new upper bound on the ALP-photon coupling $g_{a\gamma}$ is stronger than the bound from SN1987A for ALPs with masses $m_a < 3 \times 10^{-12}$ eV. Moreover, while our method is similar to that used to derive the bound from Hydra A [22], the high quality of the M87 data leads to a substantially stronger bound on $g_{a\gamma}$.

Interestingly, the values of $g_{a\gamma}$ probed by M87 are in the range of future axion experiments, such as IAXO [57] and ALPS II [58, 59], which, moreover, will be sensitive to a much wider range of ALP masses, $m_a \lesssim 10^{-2}$ – 10^{-4} eV.

Our constraint is also interesting in relation to the suggested ALP explanation of the apparent anomalous transparency of the universe for very high energy cosmic rays [19, 60–63], which postulate the existence of a light ALP with $m_a \lesssim 10^{-9}$ eV and $g_{a\gamma} \gtrsim 3 \times 10^{-12}$ GeV $^{-1}$. Our bound constrains, but does not rule out, other possible hints of light ALPs such as the soft X-ray excess from galaxy cluster which may be explained by ALP-photon conversion of a relativistic background of ALPs [14, 15, 17, 64–66], and the explanation of the possible unidentified 3.5 keV line from galaxy clusters [67, 68], which may be explained by dark matter decaying into ALPs, which subsequently convert to photons [18, 69, 70].

Finally, we note that the constraints derived in this paper also apply to other scalar particles with a dilaton-like (or Chameleon-like), $\phi F_{\mu\nu}F^{\mu\nu}$, coupling to electromagnetism. Our bound is two to three orders of magnitude stronger than earlier constraints on Chameleon-like particles from galaxy clusters [71] (see also [22]).

In conclusion, our result highlights the power of X-ray astronomy in searches for axion-like particles. We expect that complementary constraints can be obtained from other localised, bright X-ray sources, and possibly also from the thermal spectrum of cluster gas.

Acknowledgements

We would like to thank Ben Allanach and Mark Manera for stimulating discussions, and Joseph Conlon for discussions and valuable comments on the draft. DM is supported by a Stephen Hawking Advanced Fellowship at the Centre for Theoretical Cosmology, University of Cambridge. HRR and ACF acknowledges support from ERC Advanced Grant Feedback 340442. CSR thanks support from the Chandra Guest Observer Program under the Smithsonian Astrophysical Observatory grant GO617110B. Support for this work was provided by the National Aeronautics and Space Administration through Chandra Award Number GO6-17110A issued by the Chandra X-ray Observatory Center, which is operated by the Smithsonian Astrophysical Observatory for and on behalf of the National Aeronautics Space Administration under contract NAS8-03060.

A Sensitivity to background subtraction and modelling assumptions

In this appendix, we show that a naive application of the frequentist’s profile likelihood method leads to a strong hint of a light ALP at 99% confidence level from M87, but that this hint is spurious and due to overfitting statistical fluctuations. Moreover, we investigate the sensitivity of our constraint to the assumptions of the data reduction and the cluster modelling.

A.1 Profile likelihood constraints and over-fitting

For particular values of the parameters $(m_a, g_{a\gamma})$, the ALP-induced modulations are comparable in size to the statistical fluctuations of the binned X-ray data. For certain magnetic fields, the ALP-modulated AGN spectrum can then lead to a better fit than the plain absorbed power-law by over-fitting statistical fluctuations. This effect was found in a likelihood analysis of X-ray data from Hydra A to lead to a slight (1.2σ) statistical preference for a non-vanishing ALP coupling [22], which, however, should not be interpreted as evidence for a new particle. In this section, we show that this effect becomes more pronounced with improved observational data, leading in our case

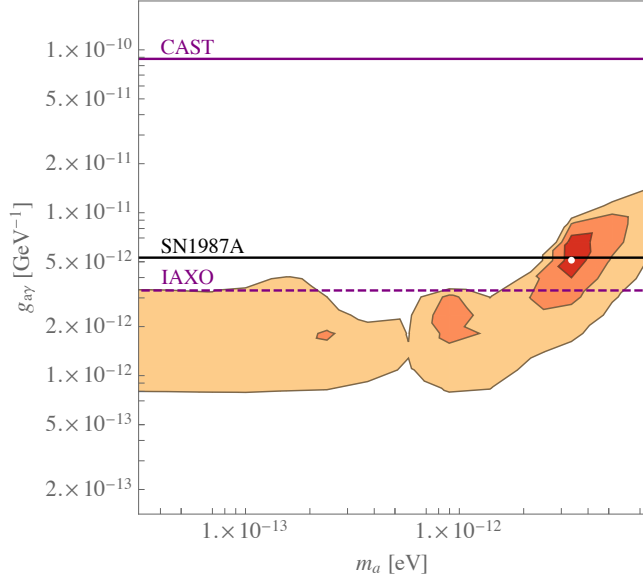


Figure 7. Profile likelihood parameter constraints at 68% (red), 95% (orange) and 99% (yellow) confidence levels; the white dot indicates the best-fit parameters.

to an apparent exclusion of a vanishing ALP-photon coupling at the 99% confidence level. We note that this limits the naive applicability of standard frequentist’s tools for constraining ALP parameters from astrophysical observations.

Assuming the existence of an ALP, its parameters can be constrained using the profile likelihood method. We here follow the prescription of [72], which we now review. We denote the X-ray observations O_i (for $i = 1, \dots, n$) and the inverse covariance matrix of these measurements by Σ^{ij} . The data is modelled by the values $C_i(\Theta)$ that depend on the model parameters Θ . The best-fit values of the parameters are obtained by minimising the χ^2 function,

$$\chi^2(\Theta) = (O_i - C_i(\Theta)) \Sigma^{ij} (O_j - C_j(\Theta)) , \quad (\text{A.1})$$

where repeated indices are summed over. The model parameters Θ include the ‘interesting’ axion parameters $\Phi = \{m_a, g_{a\gamma}\}$ as well as the (for our purposes) uninteresting parameters Ψ : these include the spectral index of the source, n_s , the hydrogen column densities for each of the observations, $n_H^{(\text{obs})}$, and the magnetic field realisation b . For a given confidence level α , the confidence region $R(\alpha)$ for Φ is determined by the axion parameters satisfying,

$$\min_{\Psi} (\chi^2(\Phi, \Psi)) - \min_{\Psi, \Phi} (\chi^2(\Phi, \Psi)) \leq \Delta(\alpha) , \quad (\text{A.2})$$

where $\Delta(\alpha)$ is determined by,

$$\text{Probability} (\chi_{\text{dim}(\Phi) \text{ d.o.f.}}^2 \leq \Delta(\alpha)) \leq \alpha. \quad (\text{A.3})$$

The results of this analysis are presented in Figure 7. The best-fit parameters are given by $m_a = 3.3 \times 10^{-12}$ eV and $g_{a\gamma} = 5.1 \times 10^{-12}$ GeV $^{-1}$, and are located just below the bound from the absence of an associated gamma-ray burst from SN1987A [10]. The survival probability $P_{\gamma \rightarrow \gamma}(E)$ of the best-fit model is given by the black curve of Figure 5. The 68% and 95% confidence level contours rather narrowly encircle the best-fit point, and even the 99% contour excludes a vanishing ALP-photon coupling, ostensibly leading to a ‘hint’ of an axion-like particle. However, this hint is spurious: the minimisation prescription of equation (A.2) selects the magnetic field profile that produces the most well-fitted modulation pattern, but the actual Virgo magnetic field is unknowable by any existing means, and may be quite different from that selected by this method. A frequentist analysis that properly takes the ‘look elsewhere’ effect into account should drastically decrease the significance of this hint, and provide constraints consistent with the Bayesian analysis in section 5.2. Figure 8 shows the best-fit ALP model together with the unmodulated power-law model. While the unmodulated power spectrum has $\chi^2 = 597$ for 614 degrees of freedom, the best-fit ALP model has $\chi^2 = 586$ for 617 degrees of freedom. The distribution of χ^2 values for different choices of the ALP parameters m_a and $g_{a\gamma}$ are shown in Figure 9. Finally, Figure 13 shows two additional ALP-distorted spectra and Figure 12 shows $P_{\gamma \rightarrow a}(E)$ for four random realisation of the cluster magnetic field, and nine choices of the ALP parameters.

A.2 Bayesian model comparison

One way to compare how well the data fits the ALP model, which we will denote \mathcal{M}_1 , and the unmodulated, no-ALP model, \mathcal{M}_0 , is to compute the corresponding Bayes factor (for a recent review of Bayesian statistics, see e.g. [73]). The data provides increased evidence for model \mathcal{M}_1 if the Bayes factor satisfies,

$$B_{01} \equiv \frac{p(d|\mathcal{M}_0)}{p(d|\mathcal{M}_1)} < 1. \quad (\text{A.4})$$

Here, $p(d|\mathcal{M})$ denotes the Bayesian evidence,

$$p(d|\mathcal{M}) \equiv \int p(d|\Theta, \mathcal{M})p(\Theta|\mathcal{M})d\Theta, \quad (\text{A.5})$$

where $p(\Theta|\mathcal{M})$ denotes the prior probability distribution of the model parameters. For the ALP model, we have $\Theta = \{m_a, g_{a\gamma}, b\}$, while the no-ALP model has no free

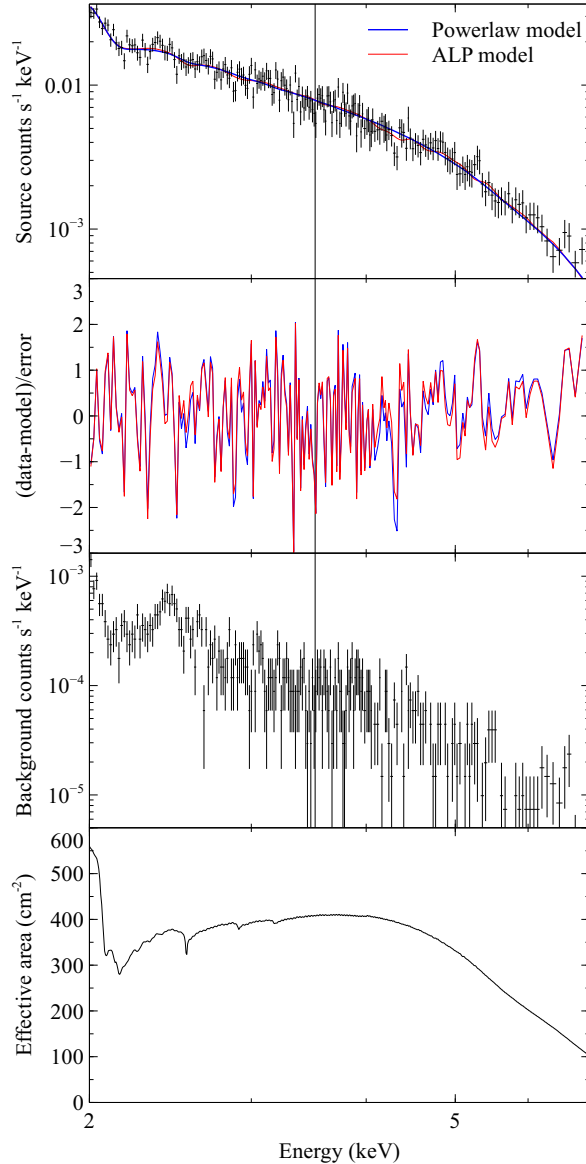


Figure 8. Comparison of the best-fit ALP model with the best-fit power-law model. The panels show the summed 2016 spectrum (see Fig. 2) with the two best-fit models, the residuals for each model, the cluster background spectrum and *Chandra*'s effective area.

parameters.⁵ Recognising our ignorance of the detailed magnetic field profile of the Virgo cluster, we take a uniform prior distribution for b . The priors of m_a and $g_{a\gamma}$ are

⁵ For simplicity, we exclude the hydrogen column density and the source spectral index from the free parameters of the model. These parameters have the same parameter space for both \mathcal{M}_0 and \mathcal{M}_1 , and are unlikely to affect the conclusions of this section.

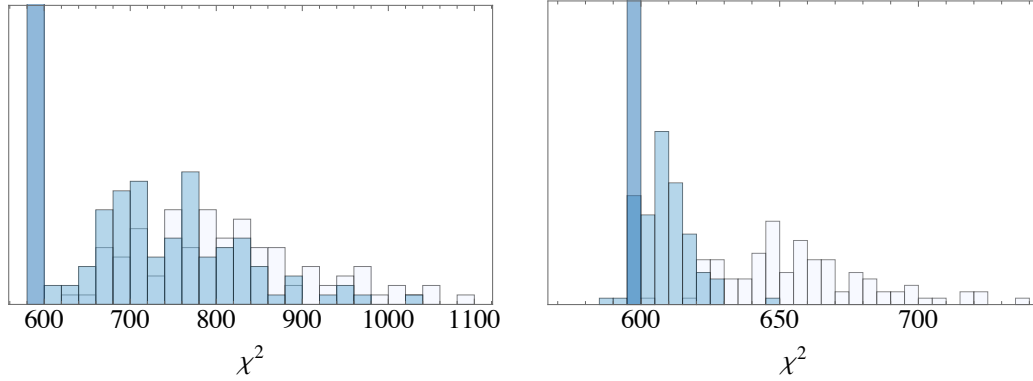


Figure 9. Distribution of χ^2 parameters for 100 realisations of the cluster magnetic field. Here, $m_a = 0$ (left) and $m_a = 3.3 \times 10^{-12}$ eV (right); $g_{a\gamma} = 1.1 \times 10^{-11}$ GeV $^{-1}$ (whitish), $g_{a\gamma} = 5.1 \times 10^{-12}$ GeV $^{-1}$ (light blue) and $g_{a\gamma} = 5 \times 10^{-13}$ GeV $^{-1}$ (darker blue). The area under each curve is the same and the dark blue column is vertically truncated for the sake of presentation.

chosen to be uniform on a log scale. We furthermore approximate the model parameters as Gaussian variables, so that the likelihoods scale like $\sim \exp(-\chi^2/2)$. We then find,

$$B_{01} = 2.0, \quad (\text{A.6})$$

which corresponds to a small increase in evidence for the no-ALP model, \mathcal{M}_0 . When interpreted, as is commonly done, against the empirical Jeffrey’s scale, this amounts to inconclusive evidence.

In sum, we have shown that a naive application of the profile likelihood method leads to a rather strong hint for a non-vanishing ALP coupling, but that both direct investigation of the corresponding best-fit model and a Bayesian model comparison point towards this hint being spurious.

A.3 Magnetic field modelling sensitivity

Radio observations of M87 and M84 constrain the magnetic field of the Virgo cluster, but they do not provide a unique solution for the magnetic field model parameters. In this section, we investigate the robustness of the constraint on the ALP parameters under certain changes in the magnetic field model.

The stochastic magnetic field model of section 3.3 has four parameters which for the benchmark model are given by,

$$(B_0, \gamma, \alpha, L_{\min}) = (31.6 \mu\text{G}, 2.5, 0.54, 1 \text{ kpc}). \quad (\text{A.7})$$

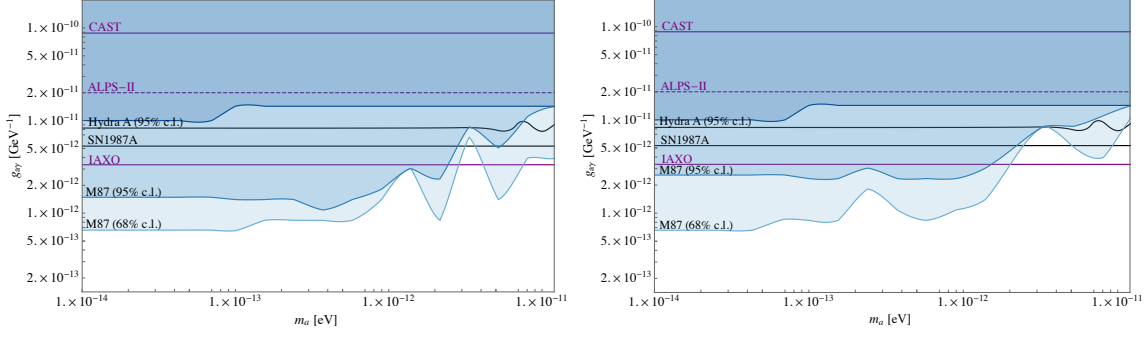


Figure 10. Parameter constraints for alternative magnetic field model 1 (left) and 2 (right) at the 68% (light blue), 95% (middle blue) and 99.7% (dark blue) confidence levels. Coloured regions are excluded.

The dependence on the central magnetic field B_0 is trivial: the transfer matrix has a symmetry $B_0 \rightarrow \lambda B_0$, $g_{a\gamma} \rightarrow g_{a\gamma}/\lambda$, and a strengthened central magnetic field corresponds to a similarly strengthened upper bound on $g_{a\gamma}$. A smaller value of γ corresponds to fewer small and more large domains, which generically increases the conversion probability. Similarly, a larger value of L_{\min} increases the ALP-photon conversion probability. Finally, a larger value of α increases the rate at which the magnetic fields falls off with radius, which suppresses the conversion probability. In section 3.3 we constrained the possible values of B_0 and α by Faraday RMs from M87 and M84. Observations of additional radio sources in or behind the Virgo cluster would further constrain the magnetic field model.

To investigate the sensitivity to the magnetic field parameters, we repeat the full analysis for two additional magnetic field models. For the first alternative magnetic field model we take $L_{\min} = 3.5$ kpc, with all other parameters as in the benchmark magnetic field model. For the second alternative magnetic field model, we take $B_0 = 35 \mu\text{G}$, $L_{\min} = 1$ kpc, and chose a steep magnetic field fall-off, $\alpha = 0.67$. As we noted in section 3.3, the benchmark value of $\alpha \approx 1/2$ can be motivated by matching the scaling of the energy density in the magnetic field to that of the gas. This value is also consistent with more elaborate magnetic field models from other clusters [74]. However, the value of $\alpha = 2/3$ may arise if the magnetic field is ‘frozen into’ the plasma, and is not excluded by Faraday rotation observations.

The corresponding parameter constraints are presented in Figure 10. The constraints from both alternative models are in good qualitative agreement with those derived from the benchmark magnetic field model, and for alternative model 1, even the upper bound on $g_{a\gamma}$ for very light ALPs is unchanged. For model 2, the steep fall-off of the magnetic field results in a slightly higher 95% contour, while the 68%

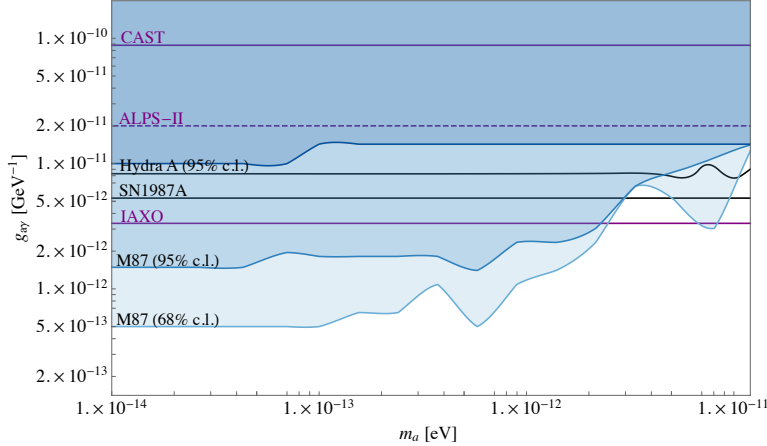


Figure 11. Original magnetic field model, 15% additional background subtraction.

contour remains essentially unchanged. Hence, we note that our constraint changes by less than a factor of two under modifications of the underlying magnetic field model, and the upper bound on $g_{a\gamma}$ is in all cases stronger than that derived from SN1987A.

A.4 Cluster background subtraction

To investigate the sensitivity of the constraints to the accuracy with which the cluster background is subtracted, we re-run the XSPEC optimisation using the observed nuclear spectrum and a 15% brighter background spectrum. Fig. 1 shows that, whilst the cluster surface brightness profile over the energy range 2 – 7 keV is approximately flat over the central few arcsec, it is also consistent with a modest increase of $\sim 10\%$ within the errors. We therefore test an increase the cluster background spectrum by a conservative value of 15%. The results are presented in Figure 11 and show that this level of uncertainty in the cluster background has a negligible effect on the ALP parameter constraints.

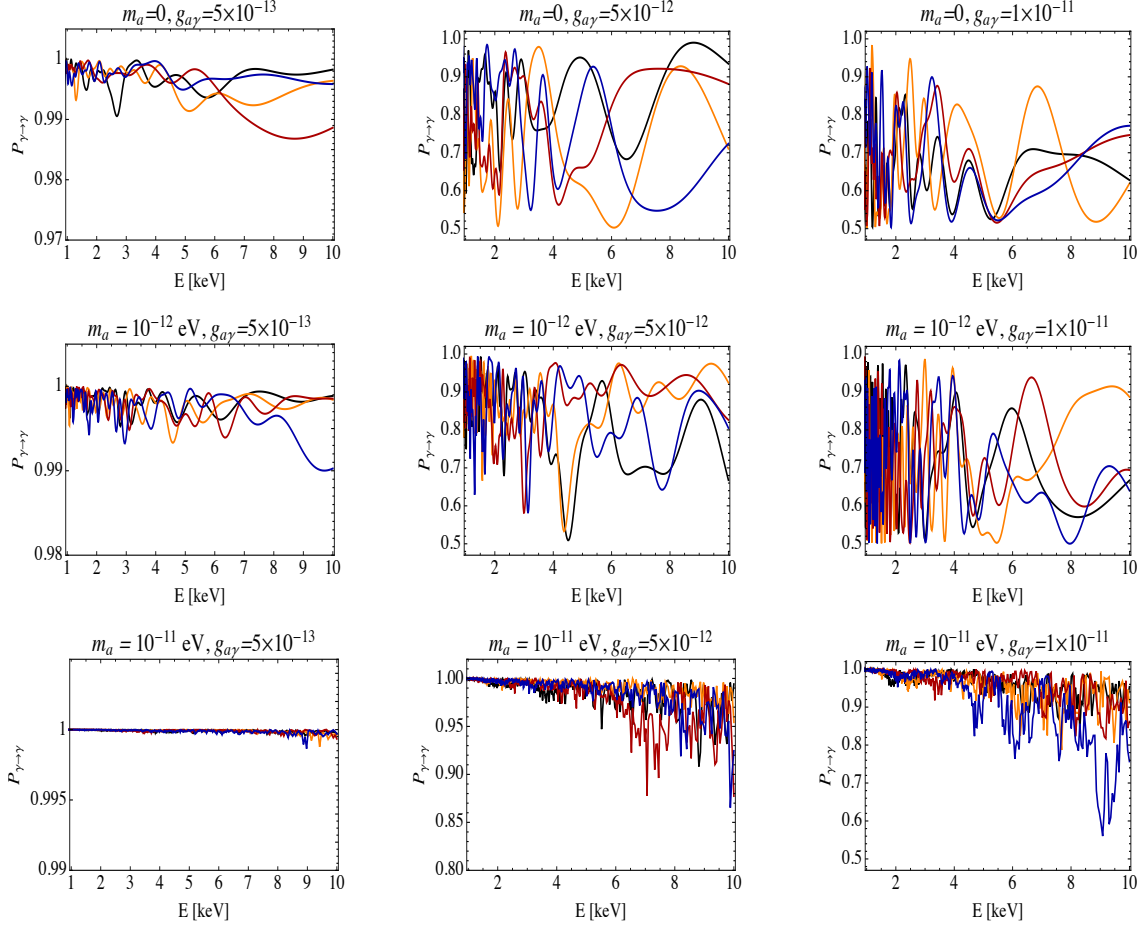


Figure 12. Conversion probability as function of energy for four random realisations of the cluster magnetic field (blue, black, orange and red), and various choices of ALP parameters.

References

- [1] S. Weinberg, *Approximate symmetries and pseudoGoldstone bosons*, *Phys. Rev. Lett.* **29** (1972) 1698–1701.
- [2] R. D. Peccei and H. R. Quinn, *CP Conservation in the Presence of Pseudoparticles*, *Phys. Rev. Lett.* **38** (1977) 1440–1443.
- [3] S. Weinberg, *A New Light Boson?*, *Phys. Rev. Lett.* **40** (1978) 223–226.
- [4] F. Wilczek, *Problem of Strong p and t Invariance in the Presence of Instantons*, *Phys. Rev. Lett.* **40** (1978) 279–282.
- [5] P. Sikivie, *Experimental Tests of the Invisible Axion*, *Phys. Rev. Lett.* **51** (1983) 1415–1417.

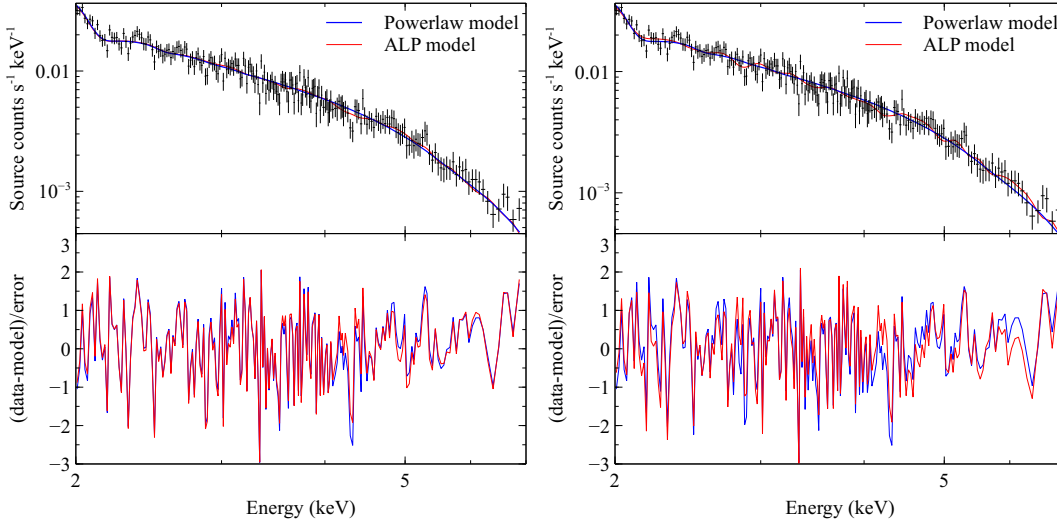


Figure 13. Comparisons of two alternative ALP models with the best-fit power-law model. The left model has $m_a = 2 \times 10^{-12}$ eV and $g_{a\gamma} = 3 \times 10^{-12}$ GeV $^{-1}$ and gives a fit with $\chi^2 = 592$, falling within the 95% contour of Figure 7. The right model has $m_a = 2 \times 10^{-12}$ eV and $g_{a\gamma} = 5 \times 10^{-12}$ GeV $^{-1}$ and gives a fit with $\chi^2 = 599$, falling just outside the 99% contour.

- [6] G. Raffelt and L. Stodolsky, *Mixing of the Photon with Low Mass Particles*, *Phys. Rev.* **D37** (1988) 1237.
- [7] P. W. Graham, I. G. Irastorza, S. K. Lamoreaux, A. Lindner and K. A. van Bibber, *Experimental Searches for the Axion and Axion-Like Particles*, *Ann. Rev. Nucl. Part. Sci.* **65** (2015) 485–514, [[1602.00039](#)].
- [8] J. W. Brockway, E. D. Carlson and G. G. Raffelt, *SN1987A gamma-ray limits on the conversion of pseudoscalars*, *Phys. Lett.* **B383** (1996) 439–443, [[astro-ph/9605197](#)].
- [9] J. A. Grifols, E. Masso and R. Toldra, *Gamma-rays from SN1987A due to pseudoscalar conversion*, *Phys. Rev. Lett.* **77** (1996) 2372–2375, [[astro-ph/9606028](#)].
- [10] A. Payez, C. Evoli, T. Fischer, M. Giannotti, A. Mirizzi and A. Ringwald, *Revisiting the SN1987A gamma-ray limit on ultralight axion-like particles*, *JCAP* **1502** (2015) 006, [[1410.3747](#)].
- [11] G. G. Raffelt, *Stars as laboratories for fundamental physics*. Chicago, USA: Univ. Pr. (1996) 664 p, 1996.
- [12] R. Essig et al., *Working Group Report: New Light Weakly Coupled Particles*, in *Proceedings, Community Summer Study 2013: Snowmass on the Mississippi (CSS2013): Minneapolis, MN, USA, July 29-August 6, 2013*, 2013. [1311.0029](#).
- [13] A. Ringwald, *Exploring the Role of Axions and Other WISPs in the Dark Universe*,

- Phys. Dark Univ.* **1** (2012) 116–135, [[1210.5081](#)].
- [14] J. P. Conlon and M. C. D. Marsh, *Excess Astrophysical Photons from a 0.1–1 keV Cosmic Axion Background*, *Phys. Rev. Lett.* **111** (2013) 151301, [[1305.3603](#)].
- [15] S. Angus, J. P. Conlon, M. C. D. Marsh, A. J. Powell and L. T. Witkowski, *Soft X-ray Excess in the Coma Cluster from a Cosmic Axion Background*, *JCAP* **1409** (2014) 026, [[1312.3947](#)].
- [16] J. P. Conlon, M. C. D. Marsh and A. J. Powell, *Galaxy cluster thermal x-ray spectra constrain axionlike particles*, *Phys. Rev.* **D93** (2016) 123526, [[1509.06748](#)].
- [17] A. J. Powell, *A Cosmic ALP Background and the Cluster Soft X-ray Excess in A665, A2199 and A2255*, *JCAP* **1509** (2015) 017, [[1411.4172](#)].
- [18] M. Cicoli, J. P. Conlon, M. C. D. Marsh and M. Rummel, *3.55 keV photon line and its morphology from a 3.55 keV axionlike particle line*, *Phys. Rev.* **D90** (2014) 023540, [[1403.2370](#)].
- [19] M. Fairbairn, T. Rashba and S. V. Troitsky, *Photon-axion mixing and ultra-high-energy cosmic rays from BL Lac type objects - Shining light through the Universe*, *Phys. Rev.* **D84** (2011) 125019, [[0901.4085](#)].
- [20] C. Burrage, A.-C. Davis and D. J. Shaw, *Active Galactic Nuclei Shed Light on Axion-like-Particles*, *Phys. Rev. Lett.* **102** (2009) 201101, [[0902.2320](#)].
- [21] D. Horns, L. Maccione, M. Meyer, A. Mirizzi, D. Montanino and M. Roncadelli, *Hardening of TeV gamma spectrum of AGNs in galaxy clusters by conversions of photons into axion-like particles*, *Phys. Rev.* **D86** (2012) 075024, [[1207.0776](#)].
- [22] D. Wouters and P. Brun, *Constraints on Axion-like Particles from X-Ray Observations of the Hydra Galaxy Cluster*, *Astrophys. J.* **772** (2013) 44, [[1304.0989](#)].
- [23] D. Wouters and P. Brun, *Irregularity in gamma ray source spectra as a signature of axionlike particles*, *Phys. Rev.* **D86** (2012) 043005, [[1205.6428](#)].
- [24] G. D’Amico and N. Kaloper, *Anisotropies in nonthermal distortions of cosmic light from photon-axion conversion*, *Phys. Rev.* **D91** (2015) 085015, [[1501.01642](#)].
- [25] M. Schlederer and G. Sigl, *Constraining ALP-photon coupling using galaxy clusters*, *JCAP* **1601** (2016) 038, [[1507.02855](#)].
- [26] M. Berg, J. P. Conlon, F. Day, N. Jennings, S. Krippendorf, A. J. Powell et al., *Searches for Axion-Like Particles with NGC1275: Observation of Spectral Modulations*, [1605.01043](#).
- [27] P. E. J. Nulsen and H. Bohringer, *A ROSAT determination of the mass of the central Virgo Cluster*, *Mon. Not. Roy. Astron. Soc.* **274** (June, 1995) 1093–1106.

- [28] O. Urban, N. Werner, A. Simionescu, S. W. Allen and H. Bohringer, *X-ray Spectroscopy of the Virgo Cluster out to the Virial Radius*, *Mon. Not. Roy. Astron. Soc.* **414** (2011) 2101, [[1102.2430](#)].
- [29] H. R. Russell, A. C. Fabian, B. R. McNamara and A. E. Broderick, *Inside the Bondi radius of M87*, *Mon. Not. Roy. Astron. Soc.* **451** (July, 2015) 588–600, [[1504.07633](#)].
- [30] F. N. Owen, J. A. Eilek and W. C. Keel, *Detection of large Faraday rotation in the inner 2 kiloparsecs of M87*, *Astrophys. J.* **362** (Oct., 1990) 449–454.
- [31] J. C. Algaba, K. Asada and M. Nakamura, *Resolving the Rotation Measure of the M87 Jet on Kiloparsec Scales*, *Astrophys. J.* **823** (June, 2016) 86, [[1603.08437](#)].
- [32] D. Guidetti, *Magnetic fields around radio galaxies from Faraday rotation measure analysis*. PhD thesis, Università di Bologna, April, 2011.
- [33] J. E. Davis, *Event Pileup in Charge-coupled Devices*, *Astrophys. J.* **562** (Nov., 2001) 575–582.
- [34] D. E. Harris, C. C. Cheung, L. Stawarz, J. A. Biretta and E. S. Perlman, *Variability Timescales in the M87 Jet: Signatures of E^2 Losses, Discovery of a Quasi Period in HST-1, and the Site of TeV Flaring*, *Astrophys. J.* **699** (July, 2009) 305–314, [[0904.3925](#)].
- [35] A. Fruscione, J. C. McDowell, G. E. Allen, N. S. Brickhouse, D. J. Burke, J. E. Davis et al., *CIAO: Chandra’s data analysis system*, in *Society of Photo-Optical Instrumentation Engineers (SPIE) Conference Series*, vol. 6270 of *Society of Photo-Optical Instrumentation Engineers (SPIE) Conference Series*, June, 2006. [DOI](#).
- [36] M. Revnivtsev, E. Churazov, S. Sazonov, W. Forman and C. Jones, *Universal X-ray emissivity of the stellar population in early-type galaxies: unresolved X-ray sources in NGC 3379*, *Astronomy and Astrophysics* **490** (Oct., 2008) 37–43, [[0804.0319](#)].
- [37] D. Jerius, *Comparison of on-axis Chandra Observations of AR Lac to SAOsc Simulations*, Oct., 2002.
- [38] K. A. Arnaud, *XSPEC: The First Ten Years*, in *Astronomical Data Analysis Software and Systems V* (G. H. Jacoby and J. Barnes, eds.), vol. 101 of *Astronomical Society of the Pacific Conference Series*, pp. 17–+, 1996.
- [39] P. M. W. Kalberla, W. B. Burton, D. Hartmann, E. M. Arnal, E. Bajaja, R. Morras et al., *The Leiden/Argentine/Bonn (LAB) Survey of Galactic HI. Final data release of the combined LDS and IAR surveys with improved stray-radiation corrections*, *Astronomy and Astrophysics* **440** (Sept., 2005) 775–782, [[arXiv:astro-ph/0504140](#)].
- [40] C. Carter, M. Karovska, D. Jerius, K. Glotfelty and S. Beikman, *ChaRT: The Chandra Ray Tracer*, in *Astronomical Data Analysis Software and Systems XII* (H. E. Payne,

- R. I. Jedrzejewski and R. N. Hook, eds.), vol. 295 of *Astronomical Society of the Pacific Conference Series*, pp. 477–+, 2003.
- [41] J. E. Davis, M. W. Bautz, D. Dewey, R. K. Heilmann, J. C. Houck, D. P. Huenemoerder et al., *Raytracing with MARX: x-ray observatory design, calibration, and support*, in *Space Telescopes and Instrumentation 2012: Ultraviolet to Gamma Ray*, vol. 8443 of *Proceedings of the SPIE*, p. 84431A, Sept., 2012. DOI.
- [42] G. C. Stewart, A. C. Fabian, P. E. J. Nulsen and C. R. Canizares, *The mass profile and gas content of M87*, *Astrophys. J.* **278** (Mar., 1984) 536–543.
- [43] A. C. Fabian, P. E. J. Nulsen and C. R. Canizares, *Cooling flows in clusters of galaxies*, *Nature* **310** (Aug., 1984) 733–740.
- [44] A. J. Young, A. S. Wilson and C. G. Mundell, *Chandra Imaging of the X-Ray Core of the Virgo Cluster*, *Astrophys. J.* **579** (Nov., 2002) 560–570, [astro-ph/0202504].
- [45] W. Forman, P. Nulsen, S. Heinz, F. Owen, J. Eilek, A. Vikhlinin et al., *Reflections of Active Galactic Nucleus Outbursts in the Gaseous Atmosphere of M87*, *Astrophys. J.* **635** (Dec., 2005) 894–906, [arXiv:astro-ph/0312576].
- [46] W. Forman, C. Jones, E. Churazov, M. Markevitch, P. Nulsen, A. Vikhlinin et al., *Filaments, Bubbles, and Weak Shocks in the Gaseous Atmosphere of M87*, *Astrophys. J.* **665** (Aug., 2007) 1057–1066, [astro-ph/0604583].
- [47] F. de Gasperin, E. Orrú, M. Murgia, A. Merloni, H. Falcke, R. Beck et al., *M 87 at metre wavelengths: the LOFAR picture*, *Astronomy and Astrophysics* **547** (Nov., 2012) A56, [1210.1346].
- [48] H. Böhringer, U. G. Briel, R. A. Schwarz, W. Voges, G. Hartner and J. Trümper, *The structure of the Virgo cluster of galaxies from Rosat X-ray images*, *Nature* **368** (Apr., 1994) 828–831.
- [49] Piffaretti, R., Jetzer, Ph. and Schindler, S., *Aspherical galaxy clusters: Effects on cluster masses and gas mass fractions*, *A&A* **398** (2003) 41–48.
- [50] E. Churazov, W. Forman, A. Vikhlinin, S. Tremaine, O. Gerhard and C. Jones, *Measuring the non-thermal pressure in early-type galaxy atmospheres: a comparison of X-ray and optical potential profiles in M87 and NGC 1399*, *Mon. Not. Roy. Astron. Soc.* **388** (Aug., 2008) 1062–1078, [0711.4686].
- [51] R. T. Zavala and G. B. Taylor, *Faraday Rotation Measures in the Parsec-Scale Jets of the Radio Galaxies M87, 3C 111, and 3C 120*, *Astrophys. J.* **566** (Feb., 2002) L9–L12, [astro-ph/0201458].
- [52] R. A. Laing and A. H. Bridle, *Rotation measure variation across M84*, *Mon. Not. Roy. Astron. Soc.* **228** (Oct., 1987) 557–571.

- [53] M. W. Kunz, A. A. Schekochihin and J. M. Stone, *Firehose and mirror instabilities in a collisionless shearing plasma*, *Phys. Rev. Lett.* **112** (May, 2014) 205003.
- [54] V. Vacca, M. Murgia, F. Govoni, L. Feretti, G. Giovannini, R. A. Perley et al., *The intracluster magnetic field power spectrum in A2199*, *Astronomy & Astrophysics* **540** (Apr., 2012) A38, [[1201.4119](#)].
- [55] W. Junor, J. A. Biretta and M. Livio, *Formation of the radio jet in M87 at 100 Schwarzschild radii from the central black hole*, *Nature* **401** (Oct., 1999) 891–892.
- [56] C. Ly, R. C. Walker and J. M. Wrobel, *An Attempt to Probe the Radio Jet Collimation Regions in NGC 4278, NGC 4374 (M84), and NGC 6166*, *Astrophys. J.* **127** (Jan., 2004) 119–124, [[astro-ph/0309743](#)].
- [57] IAXO collaboration, I. Irastorza, *The International Axion Observatory IAXO. Letter of Intent to the CERN SPS committee*, .
- [58] R. Bahre et al., *Any light particle search II – Technical Design Report*, *JINST* **8** (2013) T09001, [[1302.5647](#)].
- [59] A. Spector, *ALPS II technical overview and status report*, [1611.05863](#).
- [60] C. Csaki, N. Kaloper, M. Peloso and J. Terning, *Super GZK photons from photon axion mixing*, *JCAP* **0305** (2003) 005, [[hep-ph/0302030](#)].
- [61] M. Meyer, D. Horns and M. Raue, *First lower limits on the photon-axion-like particle coupling from very high energy gamma-ray observations*, *Phys. Rev.* **D87** (2013) 035027, [[1302.1208](#)].
- [62] G. Galanti, M. Roncadelli, A. De Angelis and G. F. Bignami, *Advantages of axion-like particles for the description of very-high-energy blazar spectra*, [1503.04436](#).
- [63] M. Meyer, D. Montanino and J. Conrad, *On detecting oscillations of gamma rays into axion-like particles in turbulent and coherent magnetic fields*, *JCAP* **1409** (2014) 003, [[1406.5972](#)].
- [64] J. P. Conlon and M. C. D. Marsh, *The Cosmophenomenology of Axionic Dark Radiation*, *JHEP* **10** (2013) 214, [[1304.1804](#)].
- [65] M. C. D. Marsh, *The Darkness of Spin-0 Dark Radiation*, *JCAP* **1501** (2015) 017, [[1407.2501](#)].
- [66] C. Evoli, M. Leo, A. Mirizzi and D. Montanino, *Reionization during the dark ages from a cosmic axion background*, *JCAP* **1605** (2016) 006, [[1602.08433](#)].
- [67] E. Bulbul, M. Markevitch, A. Foster, R. K. Smith, M. Loewenstein and S. W. Randall, *Detection of An Unidentified Emission Line in the Stacked X-ray spectrum of Galaxy Clusters*, *Astrophys. J.* **789** (2014) 13, [[1402.2301](#)].

- [68] A. Boyarsky, O. Ruchayskiy, D. Iakubovskiy and J. Franse, *Unidentified Line in X-Ray Spectra of the Andromeda Galaxy and Perseus Galaxy Cluster*, *Phys. Rev. Lett.* **113** (2014) 251301, [[1402.4119](#)].
- [69] P. D. Alvarez, J. P. Conlon, F. V. Day, M. C. D. Marsh and M. Rummel, *Observational consistency and future predictions for a 3.5 keV ALP to photon line*, *JCAP* **1504** (2015) 013, [[1410.1867](#)].
- [70] J. P. Conlon and A. J. Powell, *A 3.55 keV line from $DM \rightarrow a \rightarrow \gamma$: predictions for cool-core and non-cool-core clusters*, *JCAP* **1501** (2015) 019, [[1406.5518](#)].
- [71] A.-C. Davis, C. A. O. Schelpe and D. J. Shaw, *The Chameleonic Contribution to the SZ Radial Profile of the Coma Cluster*, *Phys. Rev.* **D83** (2011) 044006, [[1008.1880](#)].
- [72] Y. Avni, *Energy spectra of X-ray clusters of galaxies*, *Astrophys. J.* **210** (Dec., 1976) 642–646.
- [73] R. Trotta, *Bayesian Methods in Cosmology*, 2017. [1701.01467](#).
- [74] V. Vacca, *The intracluster magnetic field power spectrum in Abell 665*, in *Galaxy Clusters: Observations, Physics and Cosmology*, p. 15, July, 2010. [1001.1058](#).